



Rovibrationally Resolved Photodissociation of AlH via Excited Electronic States

Zhi Qin^{1,2} , Tianrui Bai^{1,3}, and Linhua Liu^{1,3} 

¹ Optics & Thermal Radiation Research Center, Institute of Frontier and Interdisciplinary Science, Shandong University, Qingdao, Shandong, 266237, People's Republic of China; liulinhua@sdu.edu.cn

² School of Information Science and Engineering, Shandong University, Qingdao 266237, People's Republic of China

³ School of Energy and Power Engineering, Shandong University, Jinan 250061, People's Republic of China

Received 2021 January 29; revised 2021 May 1; accepted 2021 May 27; published 2021 August 20

Abstract

Photodissociation processes are of great importance for modeling interstellar chemistry since it is a key destruction pathway for small molecules. Here, we present a detailed *ab initio* study of AlH photodissociation. Potential energy curves and transition dipole moments for AlH are obtained by using the internally contracted multireference configuration interaction method and the Davidson correction (icMRCI+Q), as well as the aug-cc-pV6Z basis set. Except for the $X^1\Sigma^+$, $A^1\Pi$, and $C^1\Sigma^+$ states, five higher excited $3^1\Sigma^+$, $2^1\Pi$, $3^1\Pi$, $4^1\Sigma^+$, and $4^1\Pi$ states are considered in order to investigate the photodissociation pathways in the vacuum ultraviolet region. State-resolved cross sections of transitions from all the rovibrational levels of the $X^1\Sigma^+$ state to seven singlet excited states are computed for photon wavelengths ranging from 500 Å to the threshold. Photodissociation cross sections in local thermal equilibrium (LTE) are obtained at temperatures from 500 to 10,000 K. Applications of the LTE cross sections to compute photodissociation rates in the standard interstellar radiation field and blackbody radiation field are briefly discussed.

Unified Astronomy Thesaurus concepts: [Astrochemistry \(75\)](#); [Molecule destruction \(2075\)](#); [Interstellar molecules \(849\)](#); [Radiative processes \(2055\)](#)

Supporting material: machine-readable tables

1. Introduction

Aluminum (Al) is a relatively abundant metallic element in interstellar space, e.g., the cosmic abundance of Al to H is 3×10^{-6} (Grevesse & Sauval 1998; Pamboundom et al. 2014). Atomic hydrogen is also quite prevalent because it is the most abundant element in the universe. Therefore, the formation of aluminum hydride (AlH) appears to be an obvious choice for a molecular Al carrier. However, AlH has remained elusive in the interstellar medium (ISM) compared to other Al-containing molecules, such as AlO, AlCl, and AlF (Pamboundom et al. 2014). Halfen & Ziurys (2010) explained that AlH spectra occur in submillimeter and infrared wavelengths, which are typically filtered by terrestrial atmospheres, therefore making them difficult to detect from ground-based observatories. Such obstacles will be resolved by Herschel, which has been successfully launched, and some upcoming space observatories, such as ESA's recently selected Atmospheric Remote-sensing Infrared Exoplanet Large-survey exoplanet characterization mission (Pascale et al. 2018) and James Webb Space Telescope (JWST; Gardner et al. 2006).

AlH has been observed in several astrophysical regions. It was detected in the stellar atmospheres of χ Cyg, a Mira variable S star, by Herbig (1956) and Herbig & Zappala (1968) and more recently in Mira variable o Ceti by Kamiński et al. (2016). AlH was also identified in sunspots by Wallace et al. (2000) through rotational lines in its $A^1\Pi$ - $X^1\Sigma^+$ electronic system, which was later analyzed for its rotational temperature by Karthikeyan et al. (2010). Herbig (1956) analyzed that the AlH might be formed by radiative association through emitting a photon in the relaxation zones of atmospheric shocks of the long-period variable star χ Cyg. The waves produce hot gases, which radiate and provide an intense radiative field, which may inversely dissociate the formed

AlH by absorbing a photon



Such a process is commonly referred to as photodissociation. The AlH detected in evolved stars could perhaps be followed up by rovibrational detection in the outer envelopes, where photodissociation is important, so photodissociation of AlH may be of interest in the future.

Photodissociation processes are found to be important for modeling the chemistry of nearly every type of astrophysical region since it is a key destruction mechanism for small molecules like AlH in photon-dominated regions (PDRs; Heays et al. 2017). Therefore, wavenumber-dependent photodissociation cross sections are required in accurate chemical modeling and in computing the photodissociation rates that are necessary to estimate the abundance of AlH. However, accurately producing the abundances of Al-bearing species is a challenging task, possibly due to the large uncertainties in kinetic data (Heays et al. 2017) and missing transition pathways (Kamiński et al. 2016). Heays et al. (2017) estimated an upper limit for photodissociation cross sections and rates of AlH using previous calculated potential energy curves (PECs) of the $A^1\Pi$ and $C^1\Sigma^+$ states, as well as electric dipole transition moments with respect to the $X^1\Sigma^+$ ground state (Matos et al. 1987). This estimation's uncertainty is within a factor of 10 (Heays et al. 2017). Moreover, both experiments (Zhu et al. 1992; Ram & Bernath 1996; Halfen & Ziurys 2004; Szajna & Zachwieja 2009; Halfen & Ziurys 2010; Szajna & Zachwieja 2010; Szajna et al. 2011, 2017) and *ab initio* calculations (Matos et al. 1987; Bauschlicher & Langhoff 1988; Scuseria et al. 1989; Wells & Lane 2011) have mainly concentrated on the low-lying $X^1\Sigma^+$ and $A^1\Pi$ states and a relatively higher $C^1\Sigma^+$ state of AlH, whereas very few studies have been carried out on higher excited states in the vacuum

ultraviolet (VUV) region, in which AlH may undergo photodissociation. A relatively detailed *ab initio* investigation of the electronic states of AlH was carried out by Wells and Lane (2011), who presented the PECs of 10 electronic states correlating to the Al (2P) + H (2S), Al (2S) + H (2S) and Al (4P) + H (2S) dissociation limits. However, the electronic states lying at higher dissociation limits and their possible photodissociation transition paths have not been investigated before. To sum up, accurate and comprehensive photodissociation cross sections of AlH remain unknown up to now and are urgently needed to compute photodissociation rates in various astronomical environments over a wide range of temperatures, e.g., from several hundred Kelvin in hot molecular cores to several thousand Kelvin in the post-shock gas and photospheres of stellar stars, and even to tens of thousands of Kelvin within the shock.

In this work, we have computed photodissociation cross sections of the AlH molecule for several electronic transitions from a wide range of initial rovibrational levels. More specifically, photodissociation cross sections of transitions from the ground $X^1\Sigma^+$ state to the $A^1\Pi$, $C^1\Sigma^+$, $3^1\Sigma^+$, $2^1\Pi$, $3^1\Pi$, $4^1\Sigma^+$, and $4^1\Pi$ states are studied here. Calculations have been performed for transitions from 1230 initial bound rovibrational levels of the $X^1\Sigma^+$ state by using quantum mechanical methods, which have become increasingly popular in computing photodissociation cross sections (Stancil et al. 1997; Weck et al. 2003a, 2003b; Loreau et al. 2011; Miyake et al. 2011; Gay et al. 2012; El-Qadi & Stancil 2013; Pamboundom et al. 2014; Babb 2015; McMillan et al. 2016; Zammit et al. 2017; Pattillo et al. 2018; Xu et al. 2019; Yang et al. 2020). Moreover, a Boltzmann distribution of initial rovibrational levels for the ground state is assumed to compute the cross sections in local thermodynamic equilibrium (LTE). Photodissociation rates are calculated for the standard interstellar radiation field (ISRF) and blackbody radiation field at a wide range of temperatures. The details of our theoretical methods are presented in Section 2. Results of PECs, transition dipole moments (TDMs), state-resolved cross sections, LTE cross sections, and photodissociation rates are discussed in Section 3. In Section 4, we provide our conclusions.

2. Theory and Calculations

2.1. *Ab Initio* Calculation

The state-averaged complete active space self-consistent field (SA-CASSCF) approach (Werner & Knowles 1985; Knowles & Werner 1985), followed by the internally contracted multi-reference configuration interaction method with the Davidson correction (icMRCI+Q; Knowles & Werner 1988; Werner & Knowles 1988; Knowles & Werner 1992; Shamasundar et al. 2011), was used to perform the molecular structure calculations, including the potential energy and TDMs of AlH. Such calculations were implemented in the quantum chemical package MOLPRO 2015 (Werner et al. 2015, 2020). Potential energies were computed for the internuclear distances from 0.95 to 14 Å. The step sizes are 0.02 Å for the internuclear distances from 1.3 to 2.0 Å, corresponding to the equilibrium geometry of most states studied here, and 0.05 Å for the other internuclear distances.

Due to the limitation of the MOLPRO program package, it cannot take advantage of the full symmetry of non-Abelian groups. Hence, for molecules with degenerate symmetry, an

Abelian subgroup is required to be used. That is, for a diatomic molecule such as AlH with $C_{\infty v}$ symmetry, it will be substituted by C_{2v} symmetry with the order of irreducible representations being (A_1, B_1, B_2, A_2). The corresponding symmetry operations for reducing from $C_{\infty v}$ to C_{2v} are $\Sigma^+ \rightarrow A_1$, $\Sigma^- \rightarrow A_2$, $\Pi \rightarrow B_1+B_2$, and $\Delta \rightarrow A_1+A_2$, respectively. MOLPRO's order of irreducible representations is (a_1, b_1, b_2, a_2), which will be utilized to represent the number of molecular orbitals (MOs) of each symmetry for AlH in the following discussion.

The quality of an MRCI+Q calculation is sensitive to the choice of basis set and active space. In order to obtain high-quality PECs and TDMs, the large augmented correlation consistent polarized sextuplet aug-cc-pV6Z (AV6Z) Gaussian basis set (Schuchardt et al. 2007), which is well known to recover 98% of the electron correlation effects of considered atoms in molecular structure calculations (Helgaker et al. 2014), was used to describe the H and Al atoms. As for the active space, adding more virtual orbitals is a popular and necessary treatment for better relaxation of the wave functions of AlH and for improving the quality of PECs, especially for higher-lying electronic states. This work aims to present the photodissociation of AlH in the VUV region, so higher electronic states are required to be considered. We systematically tested the number of virtual orbitals added into the active space to extend the existing $X^1\Sigma^+$, $A^1\Pi$, and $C^1\Sigma^+$ states to higher excited singlet electronic states ($3^1\Sigma^+$, $2^1\Pi$, $3^1\Pi$, $4^1\Sigma^+$, and $4^1\Pi$). Electrons in inner shells (i.e., $1s2s2p$ shells of aluminum) were kept closed in the reference space, corresponding to MOs (3, 1, 1, 0). The remaining electrons were put into the active space. First, the valence MOs (3, 1, 1, 0) were used to form the active space. We found that only $X^1\Sigma^+$, $A^1\Pi$, and $C^1\Sigma^+$ states could be generated well over the whole internuclear distance. Second, we added two a_1 MOs in the active space and found that the $3^1\Sigma^+$ state was also produced well over the whole internuclear distance. Then, another two a_1 MOs were added into the active space, and the $4^1\Sigma^+$ state was then obtained over the whole internuclear distance. Similarly, we gradually increased b_1 and b_2 MOs to obtain more $^1\Pi$ states and found that adding two b_1 and two b_2 virtual MOs could well produce the $A^1\Pi$, $2^1\Pi$, $3^1\Pi$, and $4^1\Pi$ states over the whole internuclear distance. Finally, 18 MOs (10, 4, 4, 0) were considered in total. Thirteen MOs were put into the active space, including seven a_1 , three b_1 , and three b_2 , which correspond to the $1s$ shell of hydrogen and $3s3p$ shells of aluminum. Due to the lack of experimental spectroscopic data for higher-lying states, we included more σ and π orbitals into the active space to ensure the accuracy of the $3^1\Sigma^+$, $2^1\Pi$, $3^1\Pi$, $4^1\Sigma^+$, and $4^1\Pi$ states.

2.2. The Photodissociation Cross Sections

The theory of photodissociation cross sections of diatomic molecules and ions has been detailed in previous works (Kirby & Van Dishoeck 1989; Miyake et al. 2011; El-Qadi & Stancil 2013; Babb 2015; McMillan et al. 2016; Zammit et al. 2017; Pattillo et al. 2018; Yang et al. 2020). Here we present a brief overview of the calculations of state-resolved photodissociation cross sections, whose expression for an electric dipole transition from a bound state i to a free state f can be

given by

$$\sigma^{\tilde{f}i}(E_{\text{ph}}) = \frac{2\pi^2 e^2 \hbar}{m_e c} \frac{df}{dE_{\text{ph}}}, \quad (2)$$

where m_e is the mass of electrons, E_{ph} is the photon energy, and the other constants have their usual meanings.

The quantity $\frac{df}{dE_{\text{ph}}}$, often called the continuum differential oscillator strength, is defined as

$$\frac{df}{dE_{\text{ph}}} = \frac{2m_e}{3\hbar^2} E_{\text{ph}} |\langle \Phi_f(\mathbf{r}, \vec{R}) | \mathbf{r} | \Phi_i(\mathbf{r}, \vec{R}) \rangle|^2, \quad (3)$$

where $\Phi(\mathbf{r}, \mathbf{R})$ is the total molecular wave function, \mathbf{r} is the vector of electronic coordinates, and \mathbf{R} is the vector of internuclear distance. Using the definition of the fine-structure constant, $\alpha = e^2/\hbar c$, and inserting Equation (3) into Equation (2) obtains the following expression:

$$\sigma^{\tilde{f}i}(E_{\text{ph}}) = \frac{4\pi^2}{3} \alpha E_{\text{ph}} |\langle \Phi_f(\mathbf{r}, \vec{R}) | \mathbf{r} | \Phi_i(\mathbf{r}, \vec{R}) \rangle|^2. \quad (4)$$

Using the Born–Oppenheimer approximation and separating the variables for the electronic and nuclear coordinates of Φ , the electric dipole transition moment function becomes

$$D^{\tilde{f}i}(R) = \langle \phi_f(\mathbf{r}|R) | \mathbf{r} | \phi_i(\mathbf{r}|R) \rangle, \quad (5)$$

where $\phi(\mathbf{r}|R)$ is the electronic molecular wave function for a fixed R and the integration is taken over all the r . Considering the degeneracies of the rotational state, Equation (5) can be given by

$$\sigma^{\tilde{f}i}(E_{\text{ph}}) = \frac{4\pi^2}{3} \alpha E_{\text{ph}} g \sum_{J'} \left(\frac{1}{2J'' + 1} S_{J'} |D_{k'J',v''J''}^{\tilde{f}i}|^2 \right), \quad (6)$$

where $D_{k'J',v''J''}^{\tilde{f}i}$ is the matrix element of the electric dipole transition moment for absorption from the rovibrational levels $v''J''$ in electronic state i to the continuum $k'J'$ in electronic state f , with the integration taken over R , and is given by

$$D_{k'J',v''J''}^{\tilde{f}i} = \langle \chi_{k'J'}(R) | D^{\tilde{f}i}(R) | \chi_{v''J''}(R) \rangle \quad (7)$$

in which $\chi_{k'J'}(R)$ is the continuum wave function for the final electronic state f , $\chi_{v''J''}(R)$ is the bound rovibrational wave function for the initial electronic state i , $D^{\tilde{f}i}(R)$ is the TDM, and g is the degeneracy factor expressed as

$$g = \frac{2 - \delta_{0,\Lambda'+\Lambda''}}{2 - \delta_{0,\Lambda''}}, \quad (8)$$

where Λ' and Λ'' are the projections of the electronic orbital angular momentum on the internuclear axis for the final and initial electronic states, respectively. The Hönl–London factors, $S_J(J'')$ are expressed for a $\Sigma \leftarrow \Sigma$ electronic transition as

$$S_{J'}(J'') = \begin{cases} J'', & J' = J'' - 1 \quad (\text{P-branch}) \\ J'' + 1, & J' = J'' + 1 \quad (\text{R-branch}) \end{cases} \quad (9)$$

and for a $\Pi \leftarrow \Sigma$ transition as

$$S_{J'}(J'') = \begin{cases} (J'' - 1)/2, & J' = J'' - 1 \quad (\text{P-branch}) \\ (2J'' + 1)/2, & J' = J'' \quad (\text{Q-branch}) \\ (J'' + 2)/2, & J' = J'' + 1 \quad (\text{R-branch}) \end{cases} \quad (10)$$

The bound and continuum rovibrational wave functions were obtained by numerically solving the radial Schrödinger equation, respectively, with the Numerov method (Numerov 1923) and the Numerov–Cooley method (Cooley 1961). The boundary condition to solve the radial Schrödinger equation for bound states is

$$\chi_{v''J''}(0) = \chi_{v''J''}(R \rightarrow \infty) = 0, \quad (11)$$

and $\chi_{v''J''}(R)$ is normalized to unity,

$$\int_0^\infty |\chi_{v''J''}(R)|^2 dR = 1. \quad (12)$$

The boundary conditions for the continuum-state wave function $\chi_{k'J'}(R)$ are

$$\chi_{k'J'}(0) = 0, \quad (13)$$

$$\chi_{k'J'}(R \text{ large}) \approx \sqrt{\frac{2\mu}{\hbar^2 \pi k'}} \sin \left[k'R - \frac{1}{2} J' \pi + \delta_J(E') \right], \quad (14)$$

where $\delta_J(E')$ is the phase shift at the continuum energy E' , and $k' = |\mathbf{k}'|$ is the magnitude of the wavevector \mathbf{k}' and equals $\sqrt{2\mu E'}$.

If both the TDMs and photon energy are in atomic units and the cross sections are in cm^2 , the numerical value of the prefactor becomes 2.689×10^{-18} , and the state-resolved cross section for a bound-free transition from initial rovibrational level $v''J''$ is

$$\sigma_{v''J''}(E_{\text{ph}}) = 2.689 \times 10^{-18} \times E_{\text{ph}} \left(\frac{2 - \delta_{0,\Lambda'+\Lambda''}}{2 - \delta_{0,\Lambda''}} \right) \times \sum_{J'} \left(\frac{1}{2J'' + 1} S_{J'}(J'') |D_{E'J',v''J''}^{\tilde{f}i}|^2 \right). \quad (15)$$

2.3. LTE Cross Sections

In LTE, a Boltzmann distribution is assumed for the rovibrational levels of the electronic ground state. The corresponding total photodissociation cross section is expressed as a function of both temperature T and wavelength λ and is given by

$$\sigma(\lambda, T) = \sum_{v''J''} w_{v''J''} \sigma_{v''J''}, \quad (16)$$

with

$$w_{v''J''} = \frac{(2J'' + 1) \exp(-|E_{v''J''} - E_{00}|/k_b T)}{Q(T)}, \quad (17)$$

where $Q(T)$ is the rovibrational partition function expressed as

$$Q(T) = \sum_{v''J''} (2J'' + 1) \exp(-|E_{v''J''} - E_{00}|/k_b T), \quad (18)$$

in which E_J is the magnitude of the bonding energy of the rovibrational level $v''J''$ and k_b is the Boltzmann constant.

2.4. Photodissociation Rates

The photodissociation rate for a molecule in an UV radiation field is given by

$$k = \int \sigma(\lambda) I(\lambda) d\lambda, \quad (19)$$

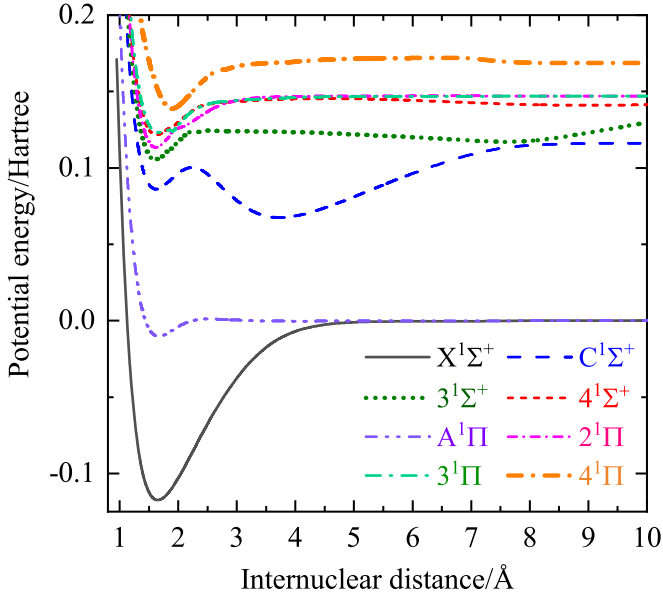


Figure 1. PECs of the eight singlet electronic states ($X^1\Sigma^+$, $A^1\Pi$, $C^1\Sigma^+$, $3^1\Sigma^+$, $2^1\Pi$, $3^1\Pi$, $4^1\Sigma^+$, and $4^1\Pi$) of AlH.

where $\sigma(\lambda)$ is the photodissociation cross section and $I(\lambda)$ is the photon radiation intensity summed over all incident angles. The photon radiation intensity surrounded by a blackbody at the temperature of T is expressed as

$$I(\lambda, T) = \frac{8\pi c/\lambda^4}{\exp(hc/k_bT\lambda) - 1}, \quad (20)$$

where h is the Planck constant, c is the speed of light, and k_b is the Boltzmann constant. In addition, the photodissociation rate under the standard ISRF is also computed using the wavelength-dependent UV intensity defined by Draine (1978), but modified for $\lambda > 2000 \text{ \AA}$ by Heays et al. (2017).

3. Results and Discussion

3.1. PECs and TDMs

By using the icMRCI+Q method, we investigated the PECs of eight electronic states of AlH, in which the $3^1\Sigma^+$, $2^1\Pi$, $3^1\Pi$, $4^1\Sigma^+$, and $4^1\Pi$ states are reported for the first time. These PECs are displayed in Figure 1 versus the internuclear distance R from 0.95 to 10 Å. A comparison of the PECs of the $X^1\Sigma^+$ and $A^1\Pi$ states with those computed by Yurchenko et al. (2018) is given in Figure 2. A good agreement can be observed for the $A^1\Pi$ state. Yurchenko et al. (2018) pointed out that the fitted PEC of the $X^1\Sigma^+$ state is higher than the dissociation limit at the long-range internuclear distances, so the calculated PEC here is reasonable. Table 1 presents the effects of different basis sets on the PECs of the ground $X^1\Sigma^+$ state. Different basis sets, including aug-cc-pVQZ (AVQZ), aug-cc-pV5Z (AV5Z), and AV6Z, appear to have a slight effect on the spectroscopic constants of the $X^1\Sigma^+$ state. But the AV6Z basis set, the largest augmented correlation consistent polarized Gaussian basis set, presents more accurate PECs because the fitted spectroscopic constants are closer to the experimental ones (Szajna et al. 2011). Compared with previous ab initio ones calculated by Wells & Lane (2011), our spectroscopic constants are closer to the experimental results (Szajna et al. 2011). Finally, we chose the AV6Z basis set to calculate the excited electronic states of AlH.

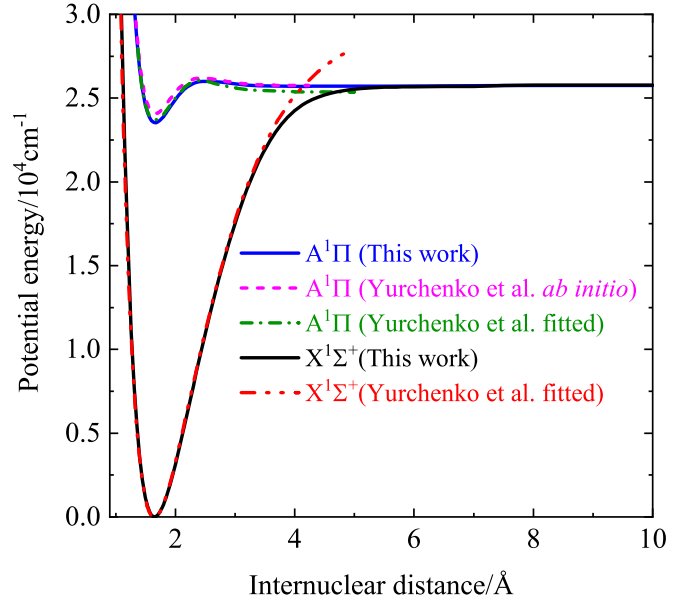


Figure 2. Comparison of the PECs of the $X^1\Sigma^+$ and $A^1\Pi$ states with those computed by Yurchenko et al. (2018).

For the $A^1\Sigma^+$ state, it has a shallow potential well that can only support two vibrational levels of 662.93 and 1776.76 cm^{-1} for $v=0$ and $v=1$, respectively. Our computed values are in reasonable agreement with the experimental ones of 666.53 and 1749.31 cm^{-1} (Szajna & Zachwieja 2009) and the theoretical values of 663.03 and 1822.81 cm^{-1} (Wells & Lane 2011), respectively. The electronic excitation energy T_e of the $A^1\Sigma^+$ state is predicted to be 23,529.19 cm^{-1} , which agrees well with that of 23,638.33 cm^{-1} observed by Szajna et al. (2011) and that of 23,959.82 cm^{-1} calculated by Wells & Lane (2011). Note that our results are slightly closer to the experimental ones than previous theoretical results.

The $C^1\Sigma^+$ state is predicted to have a double-well PEC. The minimum of the inner well is 44,621.5 cm^{-1} ($R=1.625 \text{ \AA}$) above the minimum of the ground state. The corresponding experimental minimum of the inner well is 44,675.37 cm^{-1} ($R=1.613122 \text{ \AA}$; Szajna et al. 2011). Good agreement can be observed. The minimum of the outer well is 40,595.83 cm^{-1} ($R=3.777 \text{ \AA}$) relative to the minimum of the ground state and has not been observed in the experiment. The inner well can bear two vibrational levels, which are 795.61 and 2221.65 cm^{-1} for $v=0$ and $v=1$, respectively.

The spectroscopic constants of the higher $3^1\Sigma^+$, $2^1\Pi$, $3^1\Pi$, $4^1\Sigma^+$, and $4^1\Pi$ states are fitted by the PECs and listed in Table 2. No experimental data are available to compare with them. Our calculations indicate that the $C^1\Sigma^+$ and $3^1\Sigma^+$ states have a prominent avoided crossing around 7.8 Å, which leads to the different dissociation limits for these two states (detailed below). The PECs of the $2^1\Pi$ and $3^1\Pi$ states also have an avoided crossing at R of about 1.9 Å.

Table 3 presents the dissociation relationship of the molecular states of AlH including the $X^1\Sigma^+$, $A^1\Pi$, $C^1\Sigma^+$, $3^1\Sigma^+$, $2^1\Pi$, $3^1\Pi$, $4^1\Sigma^+$, and $4^1\Pi$ states. The $X^1\Sigma^+$ and $A^1\Pi$ states converge to the first H ($1s^2S$) + Al ($3s^23p^2P$) dissociation limit. The $C^1\Sigma^+$ state correlates to the second H ($1s^2S$) + Al ($3s^24s^2S$) dissociation limit. The $2^1\Pi$ states dissociate to the fourth H ($1s^2S$) + Al ($3s^23d^2D$) asymptote. The $3^1\Pi$ and $3^1\Sigma^+$ states dissociate to the fifth H ($1s^2S$) + Al ($3s^24p^2P$) asymptote. The $4^1\Sigma^+$ state converges to the sixth H ($1s^2S$) + Al ($3s^25s^2S$) dissociation

Table 1Comparison of the Spectroscopic Constants for the Ground $X^1\Sigma^+$ State by the Present icMRCI+Q Calculation with Other Theoretical and Experimental Results

Method	R_e (Å)	T_e (cm $^{-1}$)	ω_e (cm $^{-1}$)	$\omega_e x_e$ (cm $^{-1}$)	B_e (cm $^{-1}$)	α_e (cm $^{-1}$)	D_e (eV)
MRCI+Q/aug-cc-pVQZ	1.650	0.00	1663.76	27.05	6.3609	0.1857	3.190
MRCI+Q/aug-cc-pV5Z	1.650	0.00	1664.27	26.90	6.3613	0.1858	3.201
MRCI+Q/aug-cc-pV6Z	1.650	0.00	1665.93	26.99	6.3650	0.1861	3.198
MRCI/aug-cc-pV6Z ^a	1.635	0.00	1715.39	26.01	6.4902	0.1749	
Expt. ^b	1.647	0.00	1682.37	29.05	6.3938	0.1871	3.16 ± 0.01 ^c

Notes.^a Ab initio calculations by Wells & Lane (2011).^b Szajna et al. (2011).^c Baltayan & Nedelec (1979).**Table 2**

Spectroscopic Constants Fitted by the PECs Calculated by the icMRCI/AV6Z Method

State	R_e (Å)	T_e (cm $^{-1}$)	ω_e (cm $^{-1}$)	$\omega_e x_e$ (cm $^{-1}$)	B_e (cm $^{-1}$)	α_e (cm $^{-1}$)	D_e (eV)
$3^1\Sigma^+$	1.6061	48,876.4	1727.6	124.5	6.8640	0.69833	0.506
$4^1\Sigma^+$	1.6228	52,376.9	1489.1	78.1	6.6724	0.59244	0.650
$2^1\Pi$	1.6097	50,669.2	1967.7	270.2	6.9307	0.77126	0.918
$3^1\Pi$	1.6630	52,835.7	1128.4	15.0	5.9215	0.17161	0.646
$4^1\Pi$	1.8912	56,217.5	1609.3	84.5	4.8497	0.14502	0.909

Table 3Dissociation Relationship of the $X^1\Sigma^+$, $A^1\Pi$, $C^1\Sigma^+$, $3^1\Sigma^+$, $2^1\Pi$, $3^1\Pi$, $4^1\Sigma^+$, and $4^1\Pi$ States for AlH

Molecular State	Dissociation Limit	Energy (cm $^{-1}$) ^a	Energy (cm $^{-1}$) ^b	C_5^d	C_6^d
$X^1\Sigma^+$	H ($1s^2S$) + Al ($3s^23p^2P$)	0.00	0.00	0	59.69
$A^1\Pi$	H ($1s^2S$) + Al ($3s^23p^2P$)	0.00	0.00	0	59.69
$C^1\Sigma^+$	H ($1s^2S$) + Al ($3s^24s^2S$)	25,347.756	25,306.42	0	33.77
$2^1\Pi$	H ($1s^2S$) + Al ($3s^23d^2D$)	32,435.453	32,273.25	0	24.65
$3^1\Sigma^+$	H ($1s^2S$) + Al ($3s^24p^2P$)	32,949.807	32,279.85	0	23.95
$3^1\Pi$	H ($1s^2S$) + Al ($3s^24p^2P$)	32,949.807	32,258.63	0	23.95
$4^1\Sigma^+$	H ($1s^2S$) + Al ($3s^25s^2S$)	37,689.407	32,743.31 ^c	0	17.19
$4^1\Pi$	H ($1s^2S$) + Al ($3s^2nd^2D$)	38,929.413	37,105.92	0	15.34

Notes.^a Experimental data from the NIST Atomic Spectra Database (Kramida et al. 2020).^b This work.^c The PEC of the $4^1\Sigma^+$ state is calculated until $R=17$ Å in this work. It is difficult to obtain the potential energies for $R > 17$ Å owing to the difficulty of convergence. According to Wigner–Witmer rules, the $4^1\Sigma^+$ state should dissociate to the H ($1s^2S$) + Al ($3s^25s^2S$) dissociation limit, and the PEC of the $4^1\Sigma^+$ state is predicted to go up for $R > 17$ Å in order to avoid crossing with the $3^1\Sigma^+$ state.^d Estimated. See the text for details.

limit. The $4^1\Pi$ state converges to the seventh H ($1s^2S$) + Al ($3s^2nd^2D$) dissociation limit. Note that the electronic states converging to the third H ($1s^2S$) + Al ($3s^23p^2P$) are not considered herein because they cannot undergo dipole-allowed transitions to the ground state. The relative energies of higher dissociation limits to the first dissociation limit are presented and compared with the experimental ones from the NIST Atomic Spectra Database (Kramida et al. 2020). The relative energy of the second dissociation limit is computed to be 25,561.42 cm $^{-1}$, which is only 41.336 cm $^{-1}$ (0.16%) smaller than the experimental value. The calculated relative energy of the fourth dissociation limit is 155.603 cm $^{-1}$ (0.48%) smaller than the experimental value of 32,435.453 cm $^{-1}$. As for the fifth dissociation limit, the relative energy is calculated to be 32,743.31 cm $^{-1}$, which is 206.497 cm $^{-1}$ (0.63%) smaller than the experimental value. The relative energy of the seventh dissociation limit is 823.493 cm $^{-1}$ (2%) smaller than the experimental value. Overall, the computed

relative energies of higher dissociation limits to the first dissociation limit agree reasonably with the experimental ones.

The TDMs of the radiative transitions from higher $^1\Sigma^+$ and $^1\Pi$ states to the ground $X^1\Sigma^+$ state are displayed in Figure 3. The TDM values of these seven dipole-allowed transitions are calculated from $R = 0.95$ Å to a large R where the TDM values no longer vary with increasing R . As shown in Figure 3, the TDM values for the $C^1\Sigma^+-X^1\Sigma^+$, $3^1\Sigma^+-X^1\Sigma^+$, $2^1\Pi-X^1\Sigma^+$, and $4^1\Pi-X^1\Sigma^+$ transitions become nonzero constant at large R , while the $A^1\Pi-X^1\Sigma^+$, $3^1\Pi-X^1\Sigma^+$, and $4^1\Sigma^+-X^1\Sigma^+$ transitions tend to zero at large R . Such variations of TDMs are related to the dissociated atomic states of these molecular states. For example, the $4^1\Sigma^+$ state dissociates to H ($1s^2S$) + Al ($3s^24p^2P$) and the $X^1\Sigma^+$ state dissociates to H ($1s^2S$) + Al ($3s^23p^2P$), and Al ($3s^24p^2P$) and Al ($3s^23p^2P$) have the same symmetry, which makes the TDM values of the $4^1\Sigma^+-X^1\Sigma^+$ transition tend to be zero at large R . A comparison of the TDMs for the

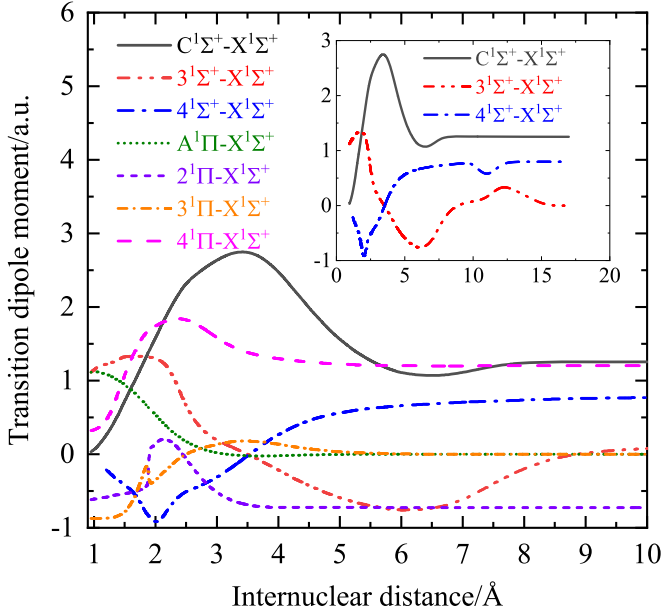


Figure 3. Transition dipole moments for the dipole-allowed transitions from the $A^1\Pi$, $C^1\Sigma^+$, $3^1\Sigma^+$, $2^1\Pi$, $3^1\Pi$, $4^1\Sigma^+$, and $4^1\Pi$ excited states to the ground $X^1\Sigma^+$ state.

$A^1\Pi-X^1\Sigma^+$ and $C^1\Sigma^+-X^1\Sigma^+$ systems with previous calculations of Bauschlicher & Langhoff (1988) and Yurchenko et al. (2018) is given in Figure 4, and a good agreement is observed. In addition, the TDMs of AlH at the long-range internuclear distance are also compared with the absolute TDMs of atomic Al deduced from the transition probabilities (Kelleher & Podobedova 2008; Papouliia et al. 2019). The estimated TDM values for transitions from Al ($3s^24s\ ^2S$), Al ($3s^23d\ ^2D$), Al ($3s^24p\ ^2P$), Al ($3s^25s\ ^2S$), and Al ($3s^2nd\ y^2D$) to the Al ground state are 1.34, 0.68, 0, 0.86, and 1.52 au, respectively. The corresponding molecular TDM values are 1.26, 0.72, 0, 0.80, and 1.22 au, respectively. A reasonable agreement can be observed.

Beyond ab initio internuclear distances (from 0.95 to 14 \AA), it is necessary to include the short- and long-range PECs and TDMs. The short-range PECs and TDMs down to an internuclear distance R of 0.5 \AA were extrapolated by the following function:

$$V(R) = A \exp(-BR) + C. \quad (21)$$

For the long-range ones up to $R = 50\ \text{\AA}$, the PECs and TDMs were extrapolated by the following formula:

$$V(R) = -\frac{C_5}{R^5} - \frac{C_6}{R^6} + V(R \rightarrow \infty), \quad (22)$$

where C_6 is the dipole–dipole dispersion coefficient, which can be estimated by the London formula

$$C_6 = \frac{3}{2} \frac{\Gamma_{Al}\Gamma_H}{\Gamma_{Al} + \Gamma_H} \alpha_{Al}\alpha_H, \quad (23)$$

where Γ is the ionization energy of each atom in a specific atomic state and α is the dipole polarizability. The ionization energies for Al and H are obtained from the NIST Atomic Spectra Database (Kramida et al. 2020). The dipole polarizability for the ground state Al ($3s^23p\ ^2P$) is 57.8 au as recommended by Schwerdtfeger & Nagle (2019). For the H ($1s\ ^2S$) state, a dipole polarizability of 4.50711 au is used

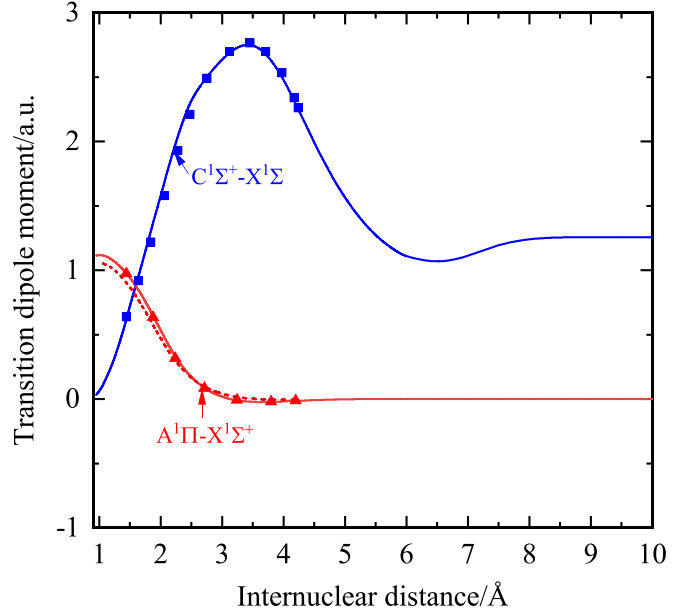


Figure 4. Transition dipole moments of the $A^1\Pi-X^1\Sigma^+$ and $C^1\Sigma^+-X^1\Sigma^+$ systems for AlH. The solid lines are from this work, the symbols represent the values from Bauschlicher & Langhoff (1988), and the dashed curve is from ab initio results computed by Yurchenko et al. (2018).

(Schwerdtfeger & Nagle 2019). As the dipole polarizabilities of different atomic states are of similar magnitude for an atom, so the α_{Al} of excited states for the Al atom are estimated as the same value of the ground Al ($3s^23p\ ^2P$) state here. Similar treatment was also adopted in the previous publication (El-Qadi & Stancil 2013). C_5 is the quadrupole–quadrupole coefficient and was estimated to be zero from Chang (1967). The estimated C_5 and C_6 are presented in Table 3.

3.2. State-resolved Cross Sections

The ground $X^1\Sigma^+$ state is found to support 33 vibrational levels, with a maximum rotational level $J'' = 72$, for a total of 1230 rovibrational levels. State-resolved photodissociation cross sections have been computed for transitions from all the rovibrational levels in the ground state to the excited electronic states of $A^1\Pi$, $C^1\Sigma^+$, $3^1\Sigma^+$, $2^1\Pi$, $3^1\Pi$, $4^1\Sigma^+$, and $4^1\Pi$, including the quasi-bound levels, at photon wavelengths from 500 \AA to the excitation threshold. Figure 5 displays the comparison of the state-resolved cross sections from the ground rovibrational level ($v'', J'' = (0, 0)$) for each transition. The cross sections of the $3^1\Pi-X^1\Sigma^+$ and $2^1\Pi-X^1\Sigma^+$ transitions have a dominant role at lower wavelengths, while the $A^1\Pi-X^1\Sigma^+$ transition plays an important part at larger wavelengths. In the region between the H Lyman photoionization limit and H Lyman α , in which the ISM radiation field is most intense, the $3^1\Pi-X^1\Sigma^+$ dominates most among these seven transitions.

Noted that the excitation energy of the last considered Al state $3s^2nd\ y^2D$ is $38929.413\ \text{cm}^{-1}$, while the ionization energy of Al is $48278.480\ \text{cm}^{-1}$. This means that we neglect some higher electronic states correlating to the dissociation limits between the H ($1s\ ^2S$) + Al ($3s^2nd\ y^2D$) and H ($1s\ ^2S$) + Al^+ ($3s^2\ ^1S_0$), which also contribute to the cross sections below a wavelength of 2572 \AA , covering a significant range of wavelengths from about 1500 \AA to the Lyman limit. Of course, if the ground-state dissociation energy is included (i.e., photodissociation from the $(v'', J'') = (0, 0)$ transitions is considered), there is a window from

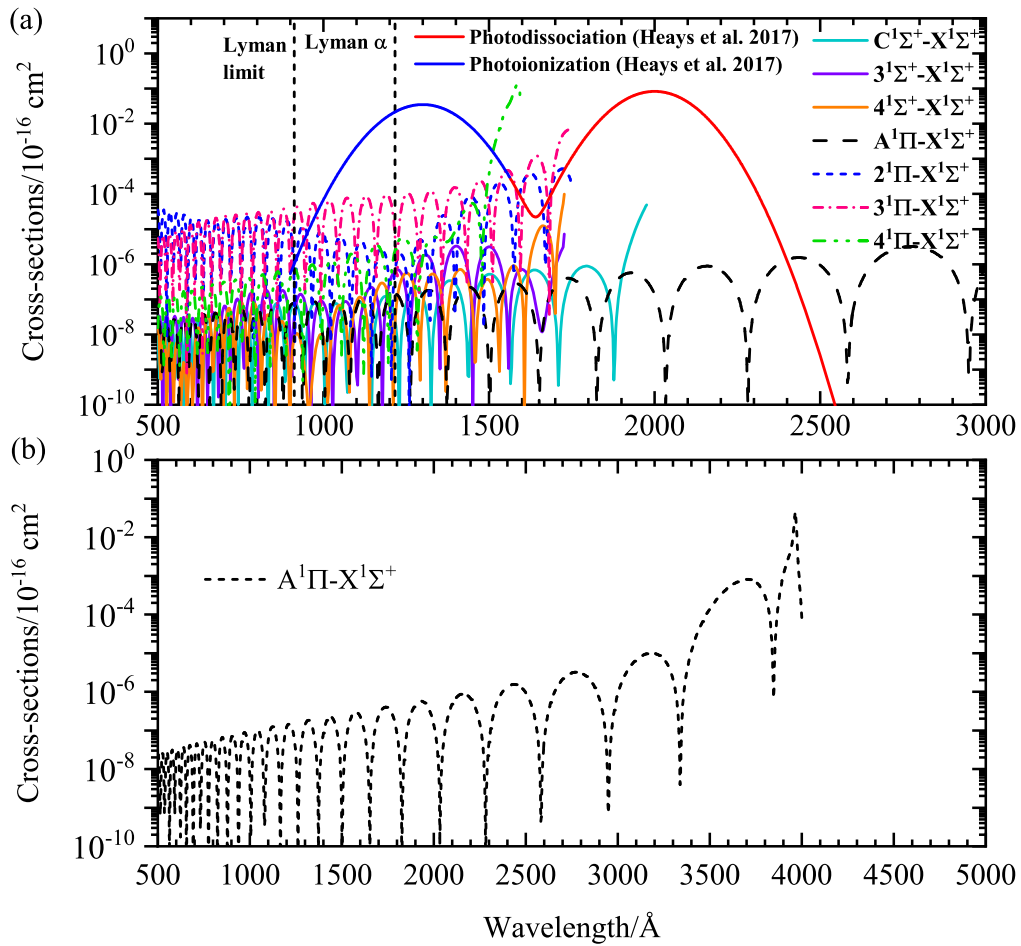


Figure 5. State-resolved cross sections of AlH for transitions from the rovibrational level $(v'', J'') = (0, 0)$ of the ground electronic state. The $C^1\Sigma^+-X^1\Sigma^+$, $3^1\Sigma^+-X^1\Sigma^+$, $4^1\Sigma^+-X^1\Sigma^+$, $A^1\Pi-X^1\Sigma^+$, $2^1\Pi-X^1\Sigma^+$, $3^1\Pi-X^1\Sigma^+$, and $4^1\Pi-X^1\Sigma^+$ transitions are shown in panel (a) at wavelengths from 500 to 2000 Å. The $A^1\Pi-X^1\Sigma^+$ transition is also solely shown in panel (b) at wavelengths from 500 to 5000 Å to exhibit its whole cross section until the excitation threshold. The photodissociation and photoionization cross sections roughly guessed by Heays et al. (2017) are also given for comparison.

about 1555 to 1357 Å where the cross-section thresholds from excited states would contribute to the total interstellar radiation. The photodissociation to the excited states correlated to the H ($n=2$) + Al ($3s^23p^2P$) dissociation limit with a threshold of about 928 Å might contribute to the cross sections as well. Moreover, it is true that there may be some bound states in the $C^1\Sigma^+$ and higher excited potentials that could result in predissociating lines at wavelengths longer than the direct photodissociation thresholds. These would be particularly important between about 1850 and 2600 Å, where the direct photodissociation cross sections are small. Hence, the photodissociation rates given in Section 3.4 are lower limits.

In addition, the photodissociation and photoionization cross sections roughly guessed by Heays et al. (2017) are presented in Figure 5(a) for comparison. The guessed photodissociation cross sections lie at wavelengths from about 1600 to 2600 Å, which may mainly come from the predissociation processes mentioned above. The photoionization cross sections are located at wavelengths longer than the Lyman limit to about 1500 Å. The direct photodissociation cross sections due to the $2^1\Pi$, $3^1\Pi$, and $4^1\Pi$ states give the largest contribution at wavelengths between about 1500 and 1800 Å. Of course, the direct photodissociation cross sections due to higher states (unconsidered here) may also exceed the contribution of photoionization for wavelengths smaller than 1500 Å.

In view of the relatively large state-resolved cross sections for the $A^1\Pi-X^1\Sigma^+$ transition at the whole wavelengths considered here, a sample of cross sections for this transition is displayed in Figure 6. Cross sections are plotted for several rotational energy levels of the ground vibrational levels $v''=0$ and for several vibrational levels at their respective lowest rotational levels $J''=0$. Transitions from initial rovibrational levels where $v''=0$ are shown in Figure 6(a) and where $J''=0$ are displayed in Figure 6(b). As expected, the cross sections shift to larger photon wavelengths owing to the decreasing photon threshold energy with increasing v'' and/or J'' .

3.3. LTE Cross Sections

LTE cross sections of each transition for AlH have been computed from 500 to 10,000 K in 50 K intervals. A comparison of LTE cross sections for each transition as a function of photon wavelength is shown in Figure 7 for $T=3000$ K. As shown in Figure 7, the $C^1\Sigma^+-X^1\Sigma^+$, $3^1\Sigma^+-X^1\Sigma^+$, $4^1\Sigma^+-X^1\Sigma^+$, $2^1\Pi-X^1\Sigma^+$, $3^1\Pi-X^1\Sigma^+$, and $4^1\Pi-X^1\Sigma^+$ transitions dominate at short wavelengths, while the $A^1\Pi-X^1\Sigma^+$ is the dominant transition at longer wavelengths. Moreover, the cross section of the $A^1\Pi-X^1\Sigma^+$ transition is dominant for the majority of the wavelengths, so the wavelength-dependent cross sections of this transition are shown in Figure 8 at several temperatures. At the same time, the

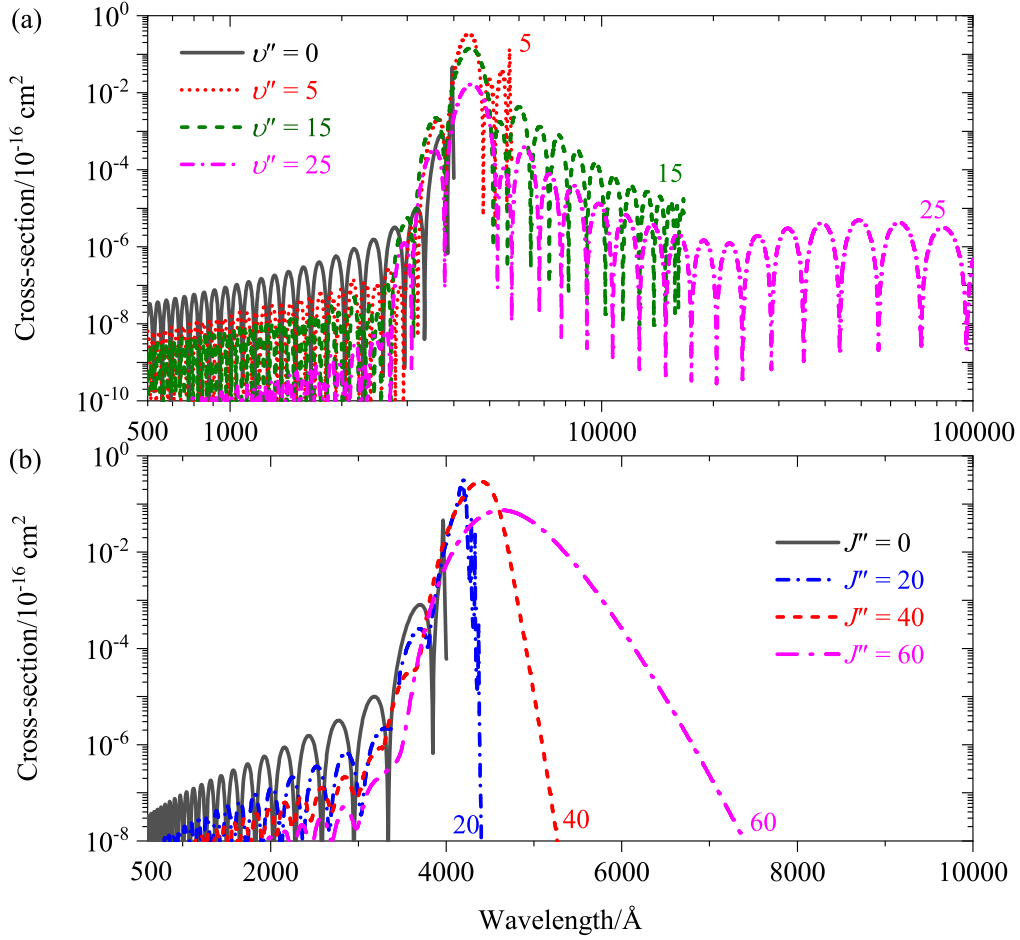


Figure 6. State-resolved cross sections for the $A^1\Pi-X^1\Sigma^+$ transition of AIH. Photodissociation transitions are given from initial rovibrational levels in which (a) $J'' = 0$ and several selected v'' and (b) $v'' = 0$ and several selected J'' .

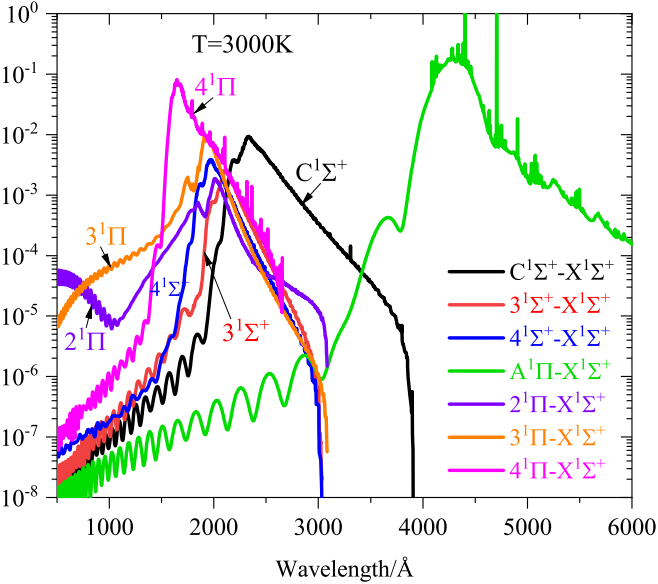


Figure 7. LTE cross sections for the seven considered photodissociation transitions of AIH at $T = 3000$ K.

state-resolved cross section for its transition from the ground rovibrational level $(v'', J'') = (0, 0)$ is included for comparison. With increasing temperature, the values of cross sections increase at longer wavelengths.

3.4. Photodissociation Rates

In general, the gas temperature is not expected to be above 100 K in the ISRF. In such situations, the gas density is usually far below the critical densities of the rovibrational levels, which means that photodissociation rates for an LTE distribution are not relevant to the ISRF. Utilizing the state-resolved cross sections from $(v'', J'') = (0, 0)$ transitions and the standard ISRF (Draine 1978; Heays et al. 2017), the AIH photodissociation rates for each electronic transition and a total contribution are calculated and listed in Table 4. The total photodissociation rate is also compared with that of Heays et al. (2017). Our calculated photodissociation rate is a factor of 2.6 smaller than that provided by Heays et al. (2017). By comparing and analyzing the photodissociation rates in Table 4, the dominant transition responsible for the photodissociation of AIH in the interstellar space is the $4^1\Pi-X^1\Sigma^+$ system, providing a contribution of about 70% of the total photodissociation from $(v'', J'') = (0, 0)$ transitions, followed by the $A^1\Pi-X^1\Sigma^+$ system, contributing about 23% of the total photodissociation.

The photodissociation rates of AIH at a blackbody radiation field are computed as well. Figure 9 highlights the AIH photodissociation rates in a blackbody radiation field for transitions from $(v'', J'') = (0, 0)$ to each excited electronic state as a function of radiation temperature. As clearly seen, the $A^1\Pi-X^1\Sigma^+$ transition dominates mostly for the whole temperature range considered here. The contribution of the $4^1\Pi-X^1\Sigma^+$ transition increases dramatically with increasing temperature.

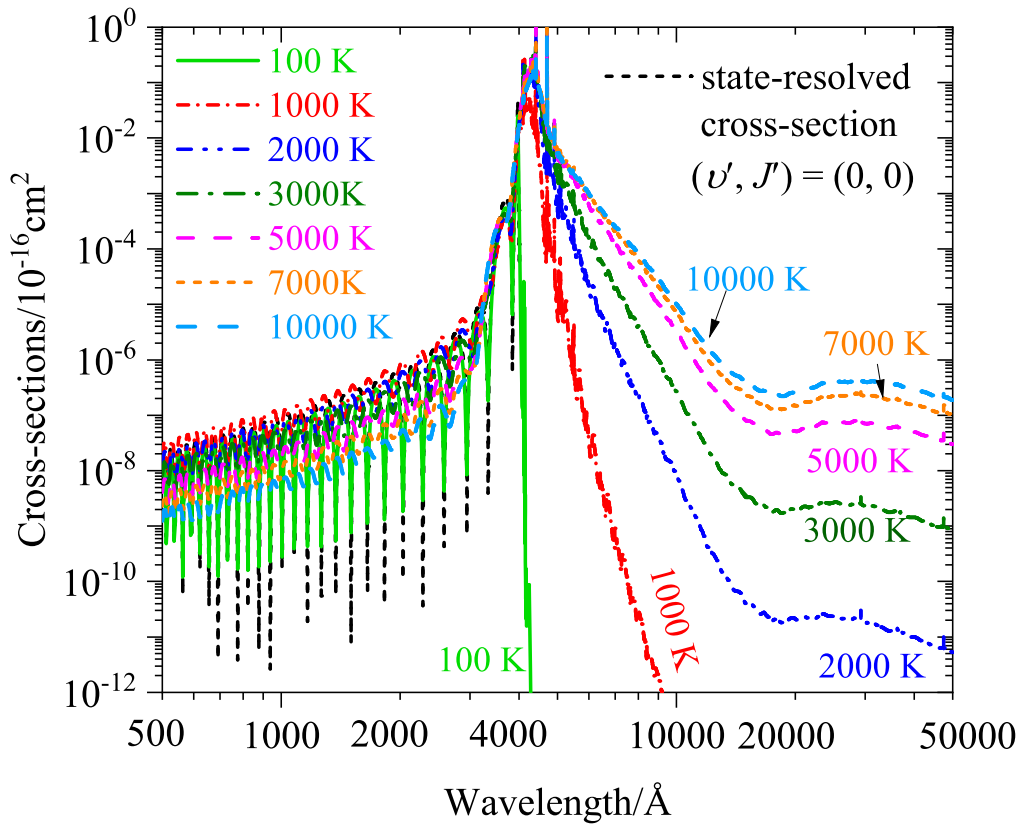


Figure 8. LTE cross sections for various kinetic temperatures for the $A^1\Pi-X^1\Sigma^+$ transition of AlH. The $(v', J') = (0, 0)$ state-resolved cross section is included as well for comparison.

Table 4

Photodissociation Rates (s^{-1}) of AlH Obtained from State-resolved Cross Sections $(v', J') = (0, 0)$ under the Standard ISRF (Draine 1978; Heays et al. 2017)

Transition	Photodissociation Rate
$C^1\Sigma^+-X^1\Sigma^+$	1.96×10^{-14}
$3^1\Sigma^+-X^1\Sigma^+$	1.12×10^{-14}
$4^1\Sigma^+-X^1\Sigma^+$	2.59×10^{-14}
All $^1\Sigma^+-X^1\Sigma^+$	5.60×10^{-14}
$A^1\Pi-X^1\Sigma^+$	2.34×10^{-11}
$2^1\Pi-X^1\Sigma^+$	5.23×10^{-13}
$3^1\Pi-X^1\Sigma^+$	5.42×10^{-12}
$4^1\Pi-X^1\Sigma^+$	7.03×10^{-11}
All $^1\Pi-X^1\Sigma^+$	9.96×10^{-11}
Total ^a	9.97×10^{-11}

Notes.

^a The total photodissociation rates are calculated from state-resolved cross section $(v', J') = (0, 0)$. The results are closer to the value of $2.6 \times 10^{-10} s^{-1}$ estimated by Heays et al. (2017) with an uncertainty of a factor of 10.

Note that the present photodissociation rates should be considered as a lower limit at the highest temperatures since photodissociation through high-lying excited states starts to become significant.

As inspired by Pattillo et al. (2018), a case is taken into account where a gas containing AlH is in LTE at a certain temperature and is situated in a blackbody radiation field at the same temperature as the gas kinetic temperature. In this case, the photodissociation rates for each transition of AlH versus the temperature are computed and depicted in Figure 10. As shown, the $A^1\Pi-X^1\Sigma^+$ transition

contributes mostly. At higher temperatures, the $C^1\Sigma^+-X^1\Sigma^+$ and $4^1\Pi-X^1\Sigma^+$ transitions become more and more important.

4. Conclusions

Photodissociation cross sections of AlH have been computed for transitions from the ground $X^1\Sigma^+$ state to the $A^1\Pi$, $C^1\Sigma^+$, $3^1\Sigma^+$, $2^1\Pi$, $3^1\Pi$, $4^1\Sigma^+$, and $4^1\Pi$ states by using ab initio PECs and TDMs, which are obtained at the icMRCI+Q/AV6Z level of theory. The state-resolved cross sections have been computed for all the rovibrational transitions from the ground electronic state of AlH. Moreover, LTE cross sections have been evaluated for seven electronic transitions at temperatures from 500 to 10,000 K. The $C^1\Sigma^+-X^1\Sigma^+$, $3^1\Sigma^+-X^1\Sigma^+$, $4^1\Sigma^+-X^1\Sigma^+$, $2^1\Pi-X^1\Sigma^+$, $3^1\Pi-X^1\Sigma^+$, and $4^1\Pi-X^1\Sigma^+$ transitions are found to be dominant at short wavelengths, while the $A^1\Pi-X^1\Sigma^+$ dominates at longer wavelengths. The resulting cross sections are appropriate to a variety of photon-dominated interstellar environments. Finally, photodissociation rates in the standard ISRF and in regions with a blackbody radiation field have been determined. We hope our theoretical work can be significantly helpful for interstellar observations.

In this work, we only studied the direct photodissociation of AlH by considering the electronic states up to the $4^1\Pi$ state. The photodissociation through these states contributes significantly at wavelengths between about 1500 and 1800 Å. The direct photodissociation due to higher states may contribute to the cross sections at wavelengths shorter than 1500 Å. The rotational interactions or spin-orbit couplings with adjacent repulsive electronic state may lead to predissociation of an electronic state of AlH, which may be very important between about 1850 and 2600 Å, where the direct photodissociation

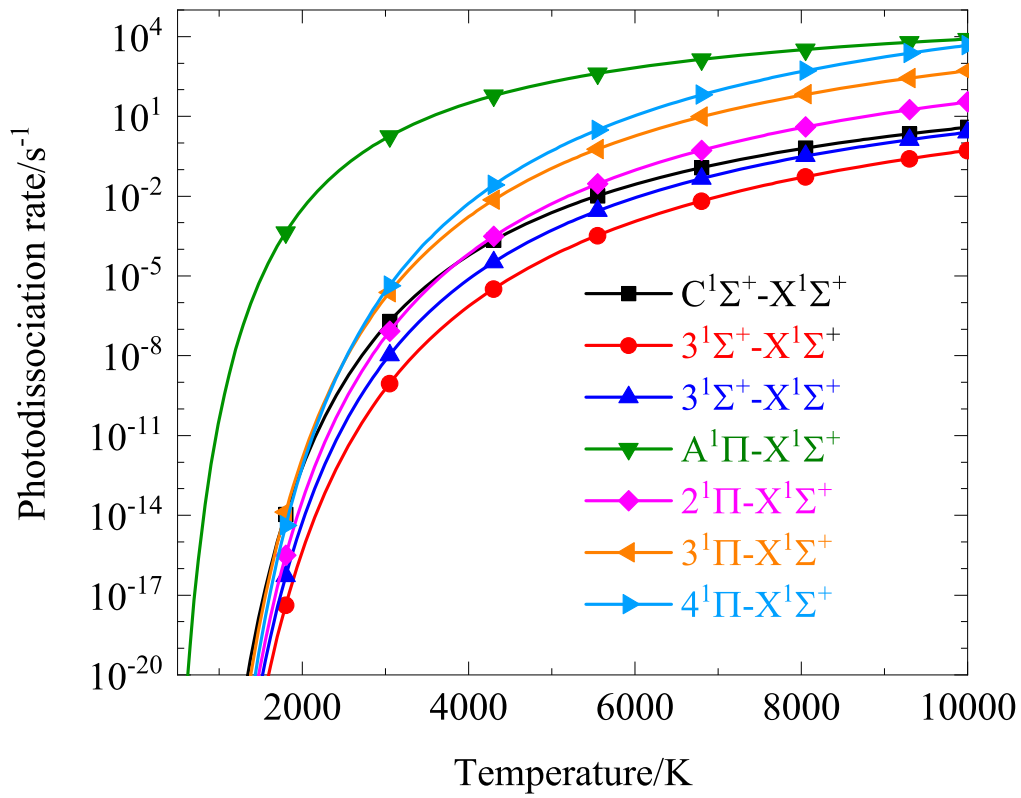


Figure 9. AIH photodissociation rates in a blackbody radiation field for transitions from $(v'', J'') = (0, 0)$ to each excited electronic state as a function of radiation temperature.

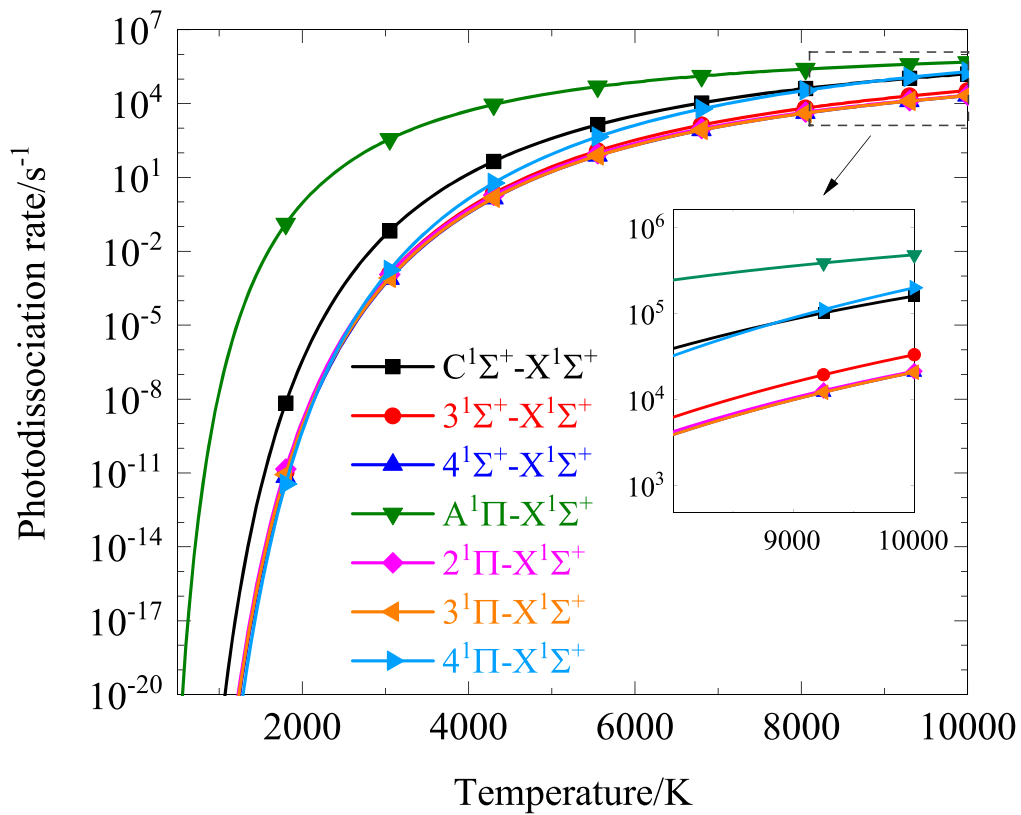


Figure 10. LTE blackbody photodissociation rates for each AIH transition as a function of temperature when the kinetic and radiation temperatures are equal.

cross sections are small. In addition, photoionization may give a contribution at wavelengths larger than the Lyman limit up to about 1500 Å. Hence, the present photodissociation rates are lower limits. Future work is required to study the contribution of the direct photodissociation from higher states and the predissociation and photoionization of AIH.

This work is sponsored by the National Natural Science Foundation of China under grant No. 51421063. This work is also supported by the Postdoctoral Applied Research Project of Qingdao. The scientific calculations in this paper have been done on the HPC Cloud Platform of Shandong University. The two referees are greatly appreciated for incisive comments, which led to considerable strengthening of this paper.

Appendix

The LTE cross sections are given in Tables A1–A8 and can also be obtained on the website.⁴

Table A1
LTE Cross Sections (cm²) for A¹Π-X¹Σ⁺ Transition of AIH

Wavelength/Å	Temperature/K			
	50	100	...	10,000
500	1.82e-24	1.65e-24		1.23e-25
503	1.87e-24	1.70e-24		1.67e-25
506	1.83e-24	1.21e-24		1.96e-25
⋮	⋮	⋮		⋮
50000	5.98e-308	2.96e-164	...	1.86e-23

(This table is available in its entirety in machine-readable form.)

Table A2
LTE Cross Sections (cm²) for 2¹Σ⁺-X¹Σ⁺ Transition of AIH

Wavelength/Å	Temperature/K			
	50	100	...	10,000
500	9.97e-25	9.63e-25		8.50e-25
503	1.78e-25	1.99e-25		8.12e-25
506	5.54e-26	5.84e-26		7.64e-25
⋮	⋮	⋮		⋮
3854	1.04e-169	2.96e-164	...	5.22e-20

(This table is available in its entirety in machine-readable form.)

Table A3
LTE Cross Sections (cm²) for 2¹Π-X¹Σ⁺ Transition of AIH

Wavelength/Å	Temperature/K			
	50	100	...	10,000
500	3.03e-21	3.09e-21		2.26e-21
503	1.64e-21	1.72e-21		2.40e-21
506	2.43e-22	2.73e-22		2.53e-21
⋮	⋮	⋮		⋮
3083	4.90e-324	1.15e-171	...	4.56e-20

(This table is available in its entirety in machine-readable form.)

Table A4
LTE Cross Sections (cm²) for 3¹Σ⁺-X¹Σ⁺ Transition of AIH

Wavelength/Å	Temperature/K			
	50	100	...	10,000
500	2.72e-24	2.47e-24		3.67e-25
503	3.80e-24	3.49e-24		4.51e-25
506	3.58e-24	3.34e-24		5.40e-25
⋮	⋮	⋮		⋮
3005	4.90e-324	3.17e-171	...	1.42e-20

(This table is available in its entirety in machine-readable form.)

Table A5
LTE Cross Sections (cm²) for 4¹Σ⁺-X¹Σ⁺ Transition of AIH

Wavelength/Å	Temperature/K			
	50	100	...	10,000
500	2.25e-24	2.11e-24		3.53e-23
503	1.11e-24	1.04e-24		4.10e-23
506	1.98e-25	2.09e-24		4.95e-23
⋮	⋮	⋮		⋮
3035	1.00e-323	4.37e-174	...	1.67e-22

(This table is available in its entirety in machine-readable form.)

Table A6
LTE Cross Sections (cm²) for 3¹Π-X¹Σ⁺ Transition of AIH

Wavelength/Å	Temperature/K			
	50	100	...	10,000
500	4.30e-22	4.53e-22		4.25e-22
503	2.31e-22	2.59e-22		4.49e-22
506	3.73e-23	4.83e-23		4.72e-22
⋮	⋮	⋮		⋮
3083	1.00e-323	4.18e-173	...	1.74e-21

(This table is available in its entirety in machine-readable form.)

Table A7
LTE Cross Sections (cm²) for 4¹Π-X¹Σ⁺ Transition of AIH

Wavelength/Å	Temperature/K			
	50	100	...	10,000
500	1.95e-23	3.14e-23		2.57e-24
503	6.97e-23	8.65e-23		3.00e-24
506	1.18e-22	1.32e-22		2.95e-24
⋮	⋮	⋮		⋮
2654	4.90e-324	6.96e-170	...	2.83e-18

(This table is available in its entirety in machine-readable form.)



Table A8
Total Cross Sections (cm²) for the Considered Transition of AIH in This Work

Wavelength/Å	Temperature/K			
	50	100	...	10,000
500	3.49e-21	3.59e-21		2.72e-21
503	1.95e-21	2.07e-21		2.89e-21
506	4.03e-22	4.59e-22		3.06e-21
⋮	⋮	⋮		⋮
50000	5.98e-308	2.96e-164	...	1.86e-23

(This table is available in its entirety in machine-readable form.)

⁴ <https://dr-zhi-qin.github.io/personal/Database.html>

ORCID iDs

Zhi Qin  <https://orcid.org/0000-0001-7995-0006>
 Linhua Liu  <https://orcid.org/0000-0002-4547-7676>

References

- Babb, J. F. 2015, *ApJS*, **216**, 21
 Baltayan, P., & Nedelec, O. 1979, *JChPh*, **70**, 2399
 Bauschlicher, C. W., & Langhoff, S. R. 1988, *JChPh*, **89**, 2116
 Chang, T. Y. 1967, *RvMP*, **39**, 911
 Cooley, J. 1961, *MaCom*, **15**, 363
 Draine, B. T. 1978, *ApJS*, **36**, 595
 El-Qadi, W., & Stancil, P. 2013, *ApJ*, **779**, 97
 Gardner, J. P., Mather, J. C., Clampin, M., et al. 2006, *SSRv*, **123**, 485
 Gay, C., Abel, N., Porter, R., et al. 2012, *ApJ*, **746**, 78
 Grevesse, N., & Sauval, A. 1998, *SSRv*, **85**, 161
 Halfen, D., & Ziurys, L. M. 2004, *ApJL*, **607**, L63
 Halfen, D., & Ziurys, L. M. 2010, *ApJ*, **713**, 520
 Heays, A., Bosman, A., & van, Van Dishoeck, E. 2017, *A&A*, **602**, A105
 Helgaker, T., Jorgensen, P., & Olsen, J. 2014, John Wiley & Sons, Molecular electronic-structure theory (Hoboken: John Wiley & Sons)
 Herbig, G. H. 1956, *PASP*, **68**, 204
 Herbig, G. H., & Zappala, R. R. 1968, *ZA*, **68**, 423
 Kamiński, T., Wong, K. T., Schmidt, M. R., et al. 2016, *A&A*, **592**, A42
 Karthikeyan, B., Rajamanickam, N., & Bagare, S. 2010, *SoPh*, **264**, 279
 Kelleher, D. E., & Podobedova, L. 2008, *JPCRD*, **37**, 709
 Kirby, K. P., & Van Dishoeck, E. F. 1989, *AdAMP*, **25**, 437
 Knowles, P. J., & Werner, H.-J. 1985, *CPL*, **115**, 259
 Knowles, P. J., & Werner, H.-J. 1988, *CPL*, **145**, 514
 Knowles, P. J., & Werner, H.-J. 1992, *AcTC*, **84**, 95
 Kramida, A., Ralchenko, Y., Reader, J. & NIST ASD Team 2020, NIST Atomic Spectra Database (version 5.8) (Gaithersburg, MD : NIST), <https://physics.nist.gov/asd>
 Loreau, J., Lecointre, J., Urbain, X., & Vaeck, N. 2011, *PhRvA*, **84**, 053412
 Matos, J. M. O., Malmqvist, P., & Roos, B. O. 1987, *JChPh*, **86**, 5032
 McMillan, E., Shen, G., McCann, J., McLaughlin, B., & Stancil, P. 2016, *JPhB*, **49**, 084001
 Miyake, S., Gay, C., & Stancil, P. 2011, *ApJ*, **735**, 21
 Numerov, B. V. 1923, *TrGla*, **2**, 188
 Pamboundom, M., Fifen, J., Nkem, C., & Nsangou, M. J. C. P. L. 2014, *CPL*, **600**, 21
 Papoulia, A., Ekman, J., & Jönsson, P. 2019, *A&A*, **621**, A16
 Pascale, E., Eccleston, P., & Tinetti, G. 2018, in 5th IEEE Int. Workshop on Metrology for AeroSpace (MetroAeroSpace). (Piscataway, NJ: IEEE), 31, doi:10.1109/MetroAeroSpace.2018.8453588
 Pattillo, R. J., Cieszewski, R., Stancil, P. C., et al. 2018, *ApJ*, **858**, 10
 Ram, R. S., & Bernath, P. F. 1996, *ApOpt*, **35**, 2879
 Schuchardt, K. L., Didier, B. T., Elsethagen, T., et al. 2007, *J. Chem Inf. Model.*, **47**, 1045
 Schwerdtfeger, P., & Nagle, J. K. 2019, *MolPh*, **117**, 1200
 Scuseria, G. E., Geertsen, J., & Oddershede, J. 1989, *JChPh*, **90**, 2338
 Shamasundar, K., Knizia, G., & Werner, H.-J. 2011, *JChPh*, **135**, 054101
 Stancil, P., Kirby, K., Sannigrahi, A., et al. 1997, *ApJ*, **486**, 574
 Szajna, W., Hakalla, R., Kolek, P., & Zachwieja, M. 2017, *JQSRT*, **187**, 167
 Szajna, W., & Zachwieja, M. 2009, *EPJB*, **55**, 549
 Szajna, W., & Zachwieja, M. 2010, *JMoSp*, **260**, 130
 Szajna, W., Zachwieja, M., Hakalla, R., & Kpa, R. 2011, *APPA*, **120**, 417
 Wallace, L., Hinkle, K., & Livingston, W. 2000, An Atlas of Sunspot Umbral Spectra in the Visible from 15 000 to 25 000 cm⁻¹ (3920 to 6664 Å). NSO Tech. Rep. 00-001 (Tucson, AZ: National Optical Astronomy Observatories)
 Weck, P., Schweitzer, A., Stancil, P., Hauschildt, P., & Kirby, K. 2003a, *ApJ*, **584**, 459
 Weck, P., Stancil, P., & Kirby, K. 2003b, *ApJ*, **582**, 1263
 Wells, N., & Lane, I. C. 2011, *PCCP*, **13**, 19018
 Werner, H. J., & Knowles, P. J. 1985, *JChPh*, **82**, 5053
 Werner, H. J., & Knowles, P. J. 1988, *JChPh*, **89**, 5803
 Werner, H. J., Knowles, P. J., Knizia, G., et al. 2015, Molpro Quantum Chemistry Software, www.molpro.net
 Werner, H.-J., Knowles, P. J., Manby, F. R., et al. 2020, *JChPh*, **152**, 144107
 Xu, Z., Luo, N., Federman, S., et al. 2019, *ApJ*, **882**, 86
 Yang, Y. K., Cheng, Y., Peng, Y. G., et al. 2020, *JQSRT*, **254**, 107203
 Yurchenko, S. N., Williams, H., Leyland, P. C., Lodi, L., & Tennyson, J. 2018, *MNRAS*, **479**, 1401
 Zammit, M. C., Savage, J. S., Colgan, J., et al. 2017, *ApJ*, **851**, 64
 Zhu, Y. F., Shehadeh, R., & Grant, E. R. 1992, *JChPh*, **97**, 883